DOI: 10.17344/acsi.2022.7570 *Acta Chim. Slov.* **2022,** *69,* 826–836

Scientific paper

Assessment of the Capability of Magnetic Nanoparticles to Recover Neodymium Ions from Aqueous Solution

Ana Ambrož,[1] Irena Ban[2] and Thomas Luxbacher[1,3,*]

[1] *University of Maribor, Faculty of Chemistry and Chemical Engineering, Laboratory for Water Biophysics and Membrane Processes, Smetanova 17, 2000 Maribor, Slovenia*

[2] *University of Maribor, Faculty of Chemistry and Chemical Engineering, Laboratory for Inorganic Chemistry, Smetanova 17, 2000 Maribor, Slovenia*

[3] *Anton Paar GmbH, Anton-Paar-Strasse 20, 8054 Graz, Austria*

* *Corresponding author: E-mail: thomas.luxbacher@anton-paar.com*

Received: 10-03-2022

Abstract

Magnetic nanoparticles (MNPs) have received increasing attention for various applications due to their fast synthesis, versatile functionalization, and recyclability by the application of a magnetic field. The high surface-to-volume ratio of MNP dispersions has suggested their use as an adsorbent for the removal of heavy metal ions. We investigated the applicability of MNPs composed of a maghemite core surrounded by a silica shell functionalized with aminopropylsilane, γ-Fe_2O_3-NH_4OH@SiO_2(APTMS), for the removal of neodymium ions (Nd^{3+}) from aqueous solution. The MNPs were characterized for their size, composition, surface functionality and charge. Despite of the promising properties of MNPs, their removal from the aqueous dispersion with an external magnet was not sufficient to reliably quantify the adsorption of Nd^{3+} by UV-Vis spectroscopy.

Keywords: Rare earth elements; Maghemite; Nanoparticles; UV-Vis spectroscopy, Adsorption

1. Introduction

The rare earth elements (REEs) are a group of 17 strongly related heavy elements that comprise scandium (Sc), yttrium (Y), lanthanum (La) and the f-block elements known as the lanthanide group, cerium (Ce) through lutetium (Lu). In addition to being of great value to general geochemistry investigations, the REEs also have high commercial value and a wide scope of applications. They are used worldwide in various electronic and optical products, in advanced technologies, medical devices, military defence systems, as well as in the field of clean energy.[1,2] REEs have been on the list of critical raw materials since 2010, and pressure on already limited resources is still increasing with the growth of the global population, industrialization, and digitalization. With regard to high economic importance and high supply risk, neodymium (Nd), europium (Eu), terbium (Tb), dysprosium (Dy), and yttrium (Y) are considered most critical.[3] With increasing demand and production, the amount of electronic waste containing REEs in various concentrations is also expanding. Sustainability in REE supply and proper treatment of end-of-life electrical and electronic compounds are crucial to achieving climate neutrality.[3] However, recycling of REEs presents many challenges. Firstly, REEs are usually present in small amounts in tiny electronic parts of gadgets like mobile phones. In some materials like touch screens, these metals are evenly distributed making them much more difficult to extract.[4] Secondly, due to the low yield and high cost of recycling processes, REEs are not recycled in large quantities, regardless of the end use. However, if REEs' prices rise, recycling may become feasible.[4,5] At present, the main focus is on the direct recycling of scrap and the urban mining, and subsequent recycling of end-of-life REE-containing products.[6]

The conventional processes for the separation and recovery of REEs mainly include precipitation, ion exchange, coagulation, flocculation, liquid–liquid extraction, biosorption, and adsorption. Among these methods, adsorption offers an efficient, environmentally friendly, and economical procedure for the removal of rare earth ions.[7,8] Among different adsorbents, magnetic nanoparti-

cles show a significant potential due to their high surface area and their response to an external magnetic field, which eases separation from a supernatant solution after completing the adsorption process.[9–11] The chemical and physical stability, biocompatibility, ease of surface modification, low toxicity, straightforward synthesis, and low cost of iron oxide nanoparticles (IONPs) make them ideal for a variety of applications.[12–15]

Preparation methods and surface coating play a key role in determining the size distribution, morphology, magnetic properties, and surface chemistry of MNPs.[16] Co-precipitation is the most widely used method for the synthesis of MNPs of controlled size and magnetic properties. It is extensively used for biomedical applications of MNPs, because of the ease of preparation and the avoidance of harmful materials and procedures.[16] Common problems in the preparation of magnetic nanoparticle dispersions are agglomeration and oxidation, which may result in the loss of dispersibility and magnetism. An additional coating of the magnetic core helps to prevent particle agglomeration and aggregation.[12] The coating method not only prevents agglomeration and oxidation of the particle, but also provides physical and chemical stability. The coating provides an interface between the magnetic nanoparticle and the surrounding environment and offers the possibility for further functionalization. The properties of the coating may markedly differ from those of the nanoparticle core.[15,17,18] Magnetic nanoparticles are commonly coated with organic (polymers or surfactants such as polyethylene glycol and dextran) or inorganic layers (gold, platinum, cobalt oxide, aluminium oxide, silica, activated carbon, etc.).[19] The coating helps to obtain a specific affinity to target molecules, to increase dispersion stability, and to improve other physicochemical properties.[9,20]

The adsorption of heavy metal ions on MNPs combined with magnetic separation has been used extensively in water treatment and environmental clean-up.[14,21] Functionalized magnetic nanoparticles act towards metal ions as a kind of "nano-sponges" and can easily be retrieved from solution with a magnet, thus they are excellent for the selective extraction of metal traces from wastewater or industrial effluents. After the adsorbed ions are stripped, the nanoparticles can be reused, making this procedure a promising sustainable green technology.[22,23] Core@shell MNPs composed of a maghemite core (γ-Fe_2O_3), and a functionalized silica coating have recently been applied for the adsorptive removal of Cu^{2+} and the rare earth ions Tb^{3+} and Dy^{3+}.[24,25]

For the adsorption of Nd^{3+} from aqueous solutions, various magnetic nanoparticles have been synthesized. Ashour et al. synthesized magnetite nanoparticles functionalized with citric acid (CA@Fe_3O_4 NPs) or l-cysteine (Cys@Fe_3O_4 NPs) for the adsorption of La^{3+}, Nd^{3+}, Gd^{3+} and Y^{3+} from aqueous solution.[26] Dupont et al. synthesized Fe_3O_4@SiO_2(TMS-EDTA) nanoparticles for the extraction and separation of different rare-earth ions.[27] Galhoum et al. used Cysteine-functionalized chitosan magnetic nanoparticles for the sorption of La^{3+}, Nd^{3+} and Yb^{3+} and hybrid chitosan magnetic nanoparticles functionalized by diethylenetriamine (DETA) for the recovery of Yb^{3+}, $Dy^{3+}$and Nd^{3+}.[28,29] Gok investigated batch adsorption method as a green technology for removal and recovery of Nd and Sm using magnetic nano-hydroxyapatite adsorbent (MNHA).[30] Li et al. prepared mesoporous magnetic Fe_3O_4@mSiO_2–DODGA nanomaterials for adsorption and recycling of REEs. The surface of mesoporous Fe_3O_4 particles was modified with a diglycolamide ligand.[31] Liu et al. worked with magnetic bio-adsorbent Fe_3O_4-C_{18}-chitosan-DETA (FCCD) composite to test the adsorption capacity of Dy^{3+}, Nd^{3+}, and Er^{3+}.[32] Miraoui et al. studied the sorption capacities of Nd^{3+} on magnetic nanoparticles grafted by poly(aminoethylene N-methyl 1-formic acid, 1-phosphonic acid) (PAEMFP).[33] Molina et al. synthesized adsorbents based on functionalized magnetite nanoparticles for the uptake of La^{3+}, Pr^{3+} and Nd^{3+} from aqueous solutions.[34]

In this paper we extend the application of γ-Fe_2O_3-NH_4OH@SiO_2 nanoparticles functionalized with aminopropyl trimethly silane (APTMS) towards the adsorption of Nd^{3+} ions from dilute aqueous solutions. To the best of our knowledge, γ-Fe_2O_3-NH_4OH@SiO_2(APTMS) magnetic nanoparticles have not been previously used for the removal of Nd^{3+} from aqueous solutions.

The monitoring of the adsorption process of dissolved heavy metal and rare-earth ions on MNPs requires the analytical detection of either the adsorbed ion concentration or the depletion of ions in solution. Aqueous solutions of Nd^{3+} appear strongly coloured and suggest the use of UV-Vis spectroscopy as a simple and reliable method for the determination of Nd^{3+} ion concentration in solution. After separation of the MNPs with an external magnet the remaining, Nd^{3+} ion concentration in the supernatant is expected to reveal the REE removal efficiency at different adsorption time. Upon a re-dispersion of the MNPs, the adsorption process may continue thereby giving fast and easy access to the characterization of the kinetics and the optimization of the adsorption process. However, the polydisperse size distribution and the stabilization of the core@shell MNPs compete with the magnetic force applied for their separation. We demonstrate that the additional separation processes of centrifugation and filtration are required for a complete removal of MNPs in order to obtain reliable information on the Nd^{3+} ion adsorption efficiency. These additional steps for MNP separation add complexity to the process and reduce the apparent benefits of REE recovery by the adsorption on MNPs.

2. Materials and Methods

Iron(II) chloride tetrahydrate ($FeCl_2{\cdot}4H_2O$), iron(III) chloride hexahydrate ($FeCl_3{\cdot}6H_2O$), and tetraethyl or-

thosilicate (TEOS) were obtained from Merck. (3-aminopropyl)trimethoxysilane (APTMS, 97%) and 2-propanol ($(CH_3)_2CHOH$, ≥ 99.8%) were obtained from Sigma Aldrich. Ethanol (C_2H_5OH) was obtained from Carlo Erba Reagents, ammonia solution (NH_4OH, 25%) from Alkaloid AD, Skopje. Potassium chloride (KCl) and nitric acid (HNO_3, ≥ 65%) were obtained from Kemika. All chemicals were used as received, without any further purification. Deionized water (dH_2O) supplied by a water purification unit (MilliporeSigma, Burlington, USA) was used throughout the experiments. Neodymium(III) oxide (Nd_2O_3) obtained from Sigma Aldrich was used for the synthesis of neodymium(III) nitrate hexahydrate ($Nd(NO_3)_3{\cdot}6H_2O$).

2. 1. Synthesis of γ-Fe_2O_3-NH_4OH@ SiO_2(APTMS)

For the preparation of the maghemite-silica core@ shell MNPs the protocol described by Kegl et al. was used.[35] In brief, the γ-Fe_2O_3 magnetic nanoparticles were obtained by a co-precipitation method. To prepare 50 mL of 0.5 M Fe^{2+}/Fe^{3+} solution in dH_2O, $FeCl_2{\cdot}4H_2O$ and $FeCl_3{\cdot}6H_2O$ were used in molar ratio 1:2. 25% ammonia solution (150 mL) was added to a round-bottomed flask and heated under reflux and constant stirring at 300 rpm. The temperature was maintained at 87 °C. Prepared 0.5 M Fe^{2+}/Fe^{3+} solution (50 mL) was added instantaneously to the reaction mixture and kept for 1 h at 87 °C and pH 10.6. The obtained black coloured precipitate was then thoroughly rinsed with dH_2O and separated from the supernatant using a permanent magnet. Rinsed γ-Fe_2O_3 particles were stabilized in 25 mL of 25% ammonia solution at 50 °C under constant stirring at 300 rpm for 24 h. The obtained particles were precipitated from the reaction mixture by a permanent magnet.

The γ-Fe_2O_3-NH_4OH particles were functionalized by SiO_2 and APTMS. 2-propanol (66 mL), dH_2O (15.42 mL), ammonia solution (1.7 mL, 25%), TEOS (0.324 mL, 99%) and APTMS (0.518 mL) were added to 4.93 mL aqueous dispersion of γ-Fe_2O_3-NH_4OH. The reaction was carried out for 24 h in a closed vessel at room temperature and stirring at 500 rpm. The γ-Fe_2O_3-NH_4OH@SiO_2(APTMS) particles were precipitated from the reaction mixture by a permanent magnet and washed two times with ethanol and dH_2O, respectively.

2. 2. Synthesis of $Nd(NO_3)_3{\cdot}6H_2O$

Neodymium nitrate hexahydrate ($Nd(NO_3)_3{\cdot}6H_2O$) was synthesised from neodymium oxide (Nd_2O_3) powder. First, a small quantity of dH_2O was added to cover the Nd_2O_3 powder, followed by HNO_3 (≥ 65%). Nd_2O_3 and HNO_3 were used in molar ratio 1:2. The solution was heated to 90 °C and mixed in a closed beaker to achieve a clear solution. When Nd_2O_3 was completely dissolved and the solution was clear, the liquid content of the mixture was evaporated at 110 °C. The collected light purple crystals were dried at room temperature.

2. 3. Adsorption Protocol

Stock solutions of 0.05 M, 0.025 M and 0.01 M $Nd(NO_3)_3{\cdot}6H_2O$ were prepared by dissolving an appropriate amount of obtained salt in dH_2O. Adsorption experiments were conducted by mixing 5 mL of the stock solution with 12 mg of magnetic nanoparticles (γ-Fe_2O_3-NH_4OH@SiO_2(APTMS)). Functionalized magnetic nanoparticles were dispersed in the stock solution by placing the sample in an ultrasonic bath (Iskra PIO, Sonis 10) for 3 hours. After the reaction time, the adsorbent was separated from the solution by an external magnet, centrifugation at 11000 rpm for 5 min (Eppendorf, centrifuge 5804 R), and filtration with 200 nm and/or 20 nm pore-size filters (Whatman, Anotop 25), to remove the remaining nanoadsorbent.

2. 4. Characterization

The thermal behaviour and stability of the magnetic nanoparticle samples was studied using a Mettler Toledo TGA/DSC1 thermogravimetric analyser in air and N_2 atmosphere, respectively, at a gas flow rate of 100 mL/min. The TGA curves with the weight pattern and heat flow were recorded as a function of temperature in the range of 25–600 °C with a heating rate of 10 °C/min, using alumina crucibles. The used MNPs were pre-dried for 24 hours at 80 °C.

The presence of 6 mol of water in $Nd(NO_3)_3{\cdot}6H_2O$ was confirmed using the same thermogravimetric analyser by direct heating in the range of 25–700 °C at a heating rate of 10 °C/min in N_2, O_2 and air atmosphere with 50 mL/min flow rate.

To confirm the formation of Nd_2O_3, X-ray diffraction (XRD) analysis was conducted after TGA analysis using an X'Pert PRO (PANalytical) X-ray diffractometer coupled with Cu K_α radiation with a wavelength of 0.15406 nm. The measurement was performed at room temperature with a time step of 100 s in the angular range of 10° to 70° with a step size of 0.034°. Fully open (2.122) X'Celerator detector was used in the measuring protocol.

The Brunauer, Emmet and Teller (BET) theory was used to determine the specific surface area of the nanoparticles by using the Micromeritics Tristar II 3020 Surface Area and Porosity system. The samples were degassed at 40°C for 24 hours prior to each measurement by using the Micromeritics FlowPrep 060 Gas Adsorption Sample Preparation Device. Specific surface area was determined in the relative pressure range of 0.05–0.3 in nitrogen gas and temperature of –195.8 °C.

A Perkin Elmer Spectrum GX ATR-FTIR spectrometer was used to confirm the grafting of the organic ligands to the surface of the MNPs. Spectra were recorded over the

range of 4000 cm^{-1} to 400 cm^{-1} in transmission mode at a resolution of 4 cm^{-1}. Samples were dried for 24 h at 80 °C, ground into a fine powder, placed on the ATR crystal, and pressed into a thick film.

Transmission electron microscopy (TEM) images were obtained to analyse the morphology and size distribution of the nanoparticles. TEM analyses were performed with a JEOL 2010F model transmission electron microscope operating at 200 kV. The sample was prepared in a water solution, dropped onto a carbon-copper grid, and dried at room temperature. Digital Micrograph and OriginPro 2015 software were used for image analysis.

Zeta potential and size of the MNPs were measured using a Malvern Zetasizer Nano ZS with automatically chosen settings. Size characterization of the samples was made by dynamic light scattering (DLS) measurements with a 4 mW He–Ne laser operating at a wavelength of 633 nm, and a detection angle of 173° (backward scattering). A disposable cuvette was filled up to 1 cm with the particle dispersion. The zeta potential was measured using a combination of electrophoresis and laser Doppler velocimetry. For all measurements, a voltage of 50 V was applied. The attenuator index and measurement position are automatically adjusted by the software. For zeta potential measurements a folded capillary cell was used. Nanoparticle titration was performed using the Malvern MPT-2 Autotitrator in parallel with the Zetasizer Nano ZS. A titration from neutral to high pH using 0.1 M NaOH was performed to determine the isoelectric point (IEP). A subsequent titration from high to low pH with 0.1 M HCl was performed to determine the reversibility of the zeta potential. The concentration of MNPs in dH_2O was 0.01% V/V.

UV-Vis absorption spectra of Nd^{3+} solutions were recorded in the range of 200–800 nm using a Varian Cary 1 UV–Vis spectrophotometer and a quartz cuvette. For the preparation of the reference sample, magnetic nanoparticles (12 mg) were added to 1 mM KCl (5 mL). After 3 hours the MNPs were separated from the solution by an external magnet, centrifugation (11000 rpm, 5 min), and filtration with 200 nm and/or 20 nm pore-size filters. As samples, 5 mL of $Nd(NO_3)_3{\cdot}6H_2O$ stock solution of different concentrations (0.05, 0.025, 0.01 M, respectively) and MNPs (12 mg) were used.

3. Results and Discussion

The results of TGA of MNPs in air (blue curve) and nitrogen (red curve) atmosphere are displayed in Fig. 1, where the mass loss in percentages of γ-Fe_2O_3-NH_4OH@SiO_2(APTMS) NPs by heating up to 600 °C is presented. The TGA curves show that the mass loss in both atmospheres occurs in one major step. In the range from 30 °C to 180 °C absorbed alcohol and water molecules evaporate from the MNPs surface. The interval from 280 °C to 600 °C is associated with the thermal decomposition of amino groups (NH_2) and the removal of the alkyl chains of silanes from the silica coating.[11,35,36] Around 550°C the transition of maghemite to hematite occurs without any mass change.[37]

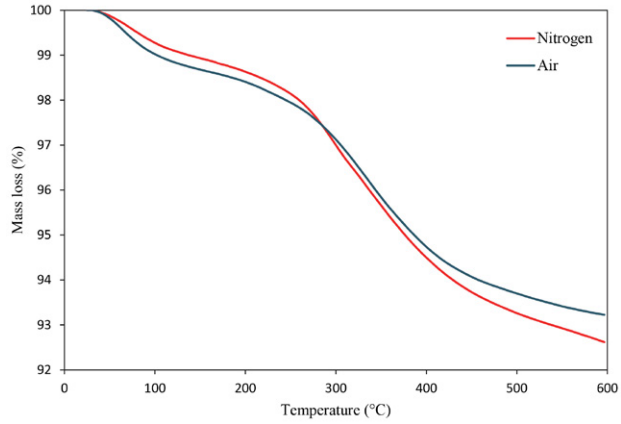

Figure 1: Mass loss of γ-Fe_2O_3-NH_4OH@SiO_2(APTMS) in N_2 and air atmosphere

The mass loss in air atmosphere corresponds to 6.7% of the sample weight. In N_2 atmosphere the mass loss presents 7.3% of the sample weight. The difference in mass loss between both atmospheres is 0.6%. Both curves show the same trend for the evolution of the mass loss with temperature. We cannot see any additional effect of oxygen on MNPs and therefore no significant sign of oxidation.

The thermal decomposition of $Nd(NO_3)_3{\cdot}6H_2O$ is a complex step-wise process, which starts with the simultaneous condensation of 6 mol of the initial monomer $Nd(NO_3)_3{\cdot}6H_2O$ into the complex $[Nd(NO_3)_3{\cdot}6H_2O]_6$. The main volatile products of the thermal decomposition are water, nitric acid, the azeotrope of 68% HNO_3 and 32% H_2O, nitrogen dioxide and oxygen.[38] The results of TGA in air (blue curve), nitrogen (red curve) and oxygen (green curve) atmosphere are displayed in Fig. 2, where the mass loss in percentages of $Nd(NO_3)_3{\cdot}6H_2O$ by heating up to 700 °C is presented.

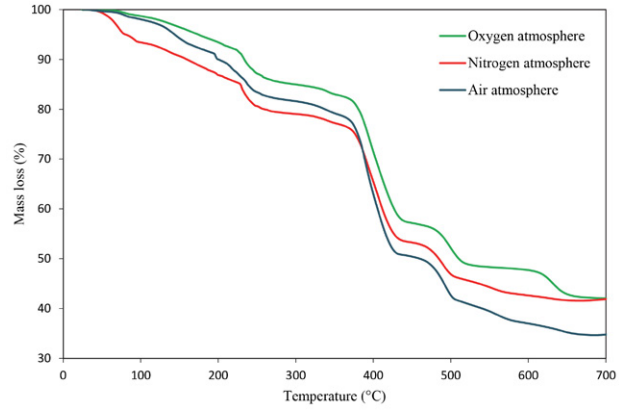

Figure 2: Mass loss of $Nd(NO_3)_3{\cdot}6H_2O$ in N_2, O_2 and air atmosphere

The thermal decomposition of samples resulted in a mass loss of 58.4% in N_2, 58.1% in O_2 and 65.2% in air atmosphere. The formation of Nd_2O_3 as the final product of TGA was confirmed with XRD analysis.

The theoretical mass loss for the thermal decomposition of $Nd(NO_3)_3{\cdot}6H_2O$ is 61.6%.[38]

There are no significant changes between oxidizing and inert atmospheres. All three curves have similar trends for the evolution of mass loss with temperature. The decomposition occurs in multiple steps, regardless of the atmosphere.

The stepwise mass loss in N_2 atmosphere is explained in accordance with the experimental results.[38] The first mass loss up to 62 °C reflects the evaporation of water during melting of the hexahydrate. It constitutes 2%, that corresponds to 3 mol of water out of 6 mol available at the beginning of the decomposition process, which are eliminated during evaporation. In the 62–358 °C range, the mass loss is 21.1%, representing the removal of 14 mol of H_2O and 5 mol of HNO_3. The next mass loss is 23.3% and it takes place in the range of 358–436 °C with the removal of 1 mol HNO_3, 5 mol of H_2O and 10 mol of NO_2. In the range of 436–513 °C 6 mol of H_2O and 2 mol of NO_2 are removed, constituting the mass loss of 7.6%. The final mass loss equals 4.4% and takes place in the range of 513–660 °C where 5 mol of H_2O and 1 mol of O_2 are removed. The remaining mass becomes constant at around 660 °C. The sum of the partial losses yields 58.4% and the presence of 6 mol of water in $Nd(NO_3)_3{\cdot}6H_2O$ was confirmed.

The BET analysis gave specific surface area of 78.27 m^2/g for γ-Fe_2O_3-NH_4OH@SiO_2(APTMS). BJH adsorption average pore width for γ-Fe_2O_3-NH_4OH@SiO_2(APTMS) is 14.07 nm and desorption average pore width is 13.85 nm with total pore volume of 0.32 cm^3/g.

Infrared spectra of synthesized nanoparticles γ-Fe_2O_3-NH_4OH (black spectrum), γ-Fe_2O_3-NH_4OH@SiO_2(APTMS) (blue spectrum) and Nd^{3+}/ γ-Fe_2O_3-NH_4OH@SiO_2(APTMS) (green spectrum) are shown in Fig. 3.

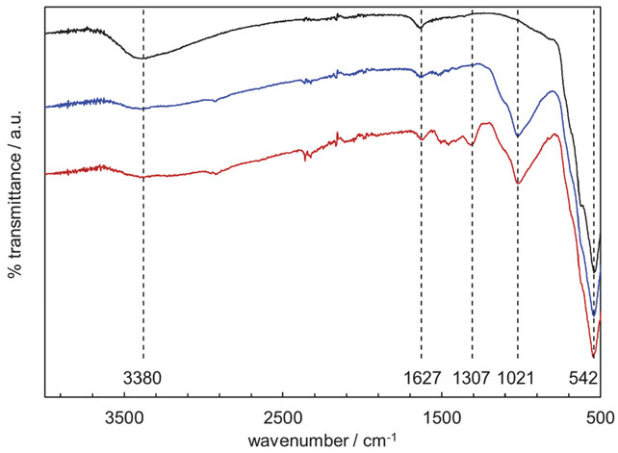

Figure 3: ATR-FTIR spectra of γ-Fe_2O_3-NH_4OH (top curve, black), γ-Fe_2O_3-NH_4OH@SiO_2(APTMS) (middle curve, blue) and Nd^{3+}/ γ-Fe_2O_3-NH_4OH@SiO_2(APTMS) (bottom curve, green)

The absorption peak at 3380.21 cm^{-1}, attributed to N-H and O-H bonds, is observed in all spectra and it is the broadest band. By comparing the spectra of the coated and the uncoated MNPs, it is observed that the band at 3380.21 cm^{-1} is less pronounced and shallower for the coated nanoparticles than for the γ-Fe_2O_3-NH_4OH nanoparticles, indicating the presence of the SiO_2 shell. The presence of Nd^{3+} on coated MNPs is visible by an even reduced intensity of the peak at 3380.21 cm^{-1}, which indicates a successful adsorption of Nd^{3+} ions on MNPs. The absorption band observed at 1627.39 cm^{-1} is found in all three samples and corresponds to the N-H bending vibration. The peak found at 1020.92 cm^{-1} corresponds to the asymmetric stretching vibration of the Si-O-Si bond and confirms the silanol functional groups grafted on the surface of γ-Fe_2O_3-NH_4OH particles. The peak observed at 542.16 cm^{-1} belongs to the stretching vibration of Fe-O, which confirms the presence of the magnetic core. When comparing uncoated and coated MNPs this peak shifts from 540.46 cm^{-1} to 542.16 cm^{-1}.

When Nd^{3+} is complexed with γ-Fe_2O_3-NH_4OH@SiO_2(APTMS) nanoparticles, a new peak at 1307.39 cm^{-1} could be observed in the spectrum. Due to the adsorption of Nd^{3+} two peaks shift to a higher wavenumber. The peak at 542.16 cm^{-1}, which corresponds to the stretching vibration of Fe-O, is shifted to 548.99 cm^{-1}. The peak at 1020.92 cm^{-1}, which corresponds to the asymmetric stretching vibration of the Si-O-Si bond, is shifted to 1022.44 cm^{-1}. The ATR-FTIR absorption spectra confirm the composition of the synthesised magnetic nanoparticles, the successful coating with SiO_2(APTMS), and the adsorption of Nd^{3+}.

The TEM photos in Fig. 4 A-C display the morphology of the MNPs with increasing magnification.

The magnetic nanoparticles have a diameter ranging between 2.5 nm and 22.5 nm, with an average particle size of 9.5 ± 1.9 nm (Fig. 4 D). This value is an estimate of size, analysed from 81 particles, as it is difficult to determine the real size of individual particles due to agglomerates and blurred boundaries between particles. Aggregation of particles results in wider size variation. None of the crystalline particles are ideally spherical, as their surface ends with a crystal plane, which is not curved. If nanoparticles are formed in a way that they can achieve an equilibrium structure, they will assume an octahedral form. But since the precipitation is an instantaneous process, we usually get incomplete shapes, which are somewhere in between a sphere and an octahedron. As shown in Fig. 4 C the particle is octahedral, but because of orientation and 2D projection of TEM images it looks like a hexagon. In Fig. 4 B and C a surface layer of amorphous SiO_2 is visible surrounding the Fe_2O_3 core, which confirms the successful coating of the MNPs.

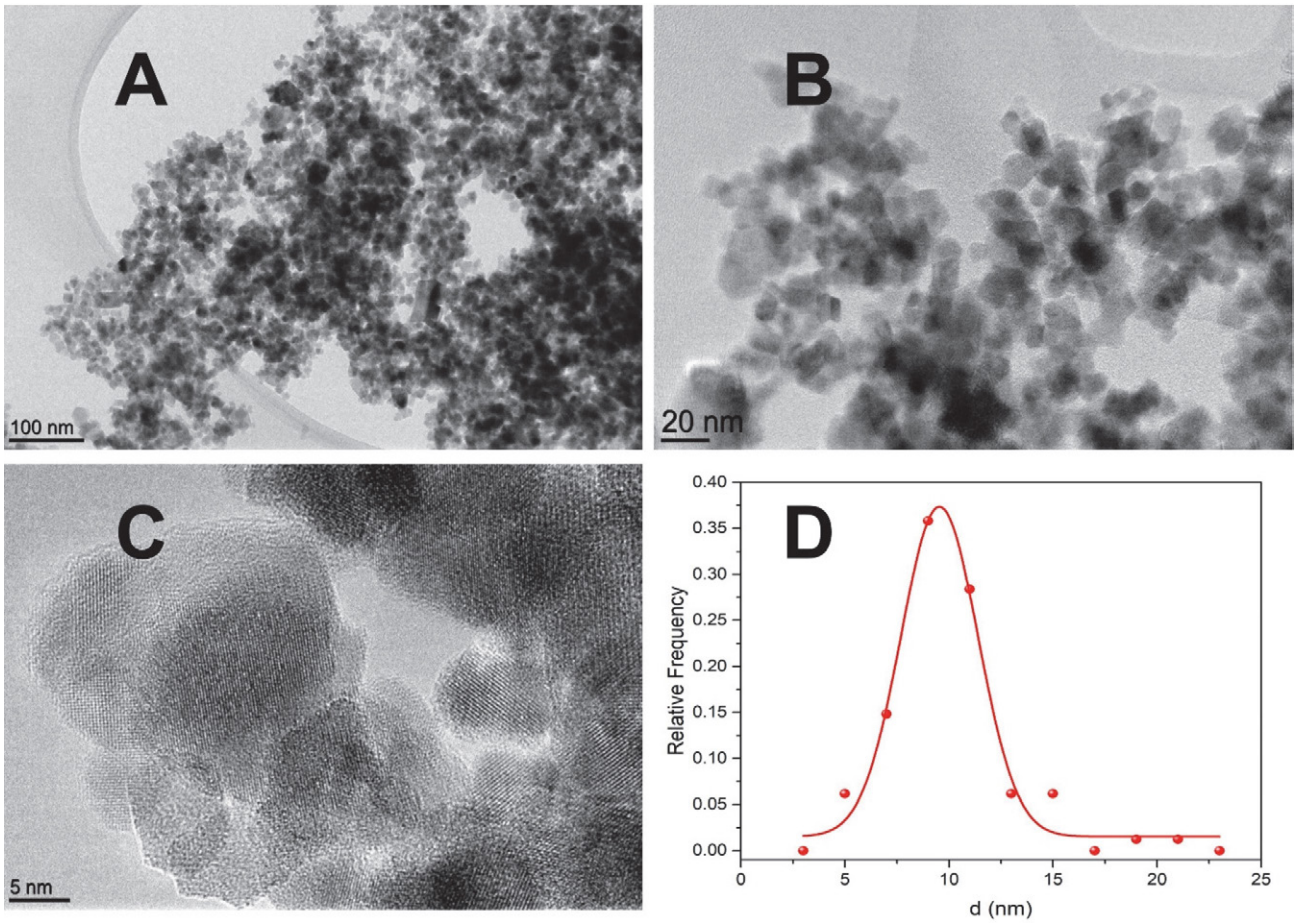

Figure 4: TEM images of γ-Fe_2O_3-NH_4OH@SiO_2(APTMS) with increasing magnification (A: scale bar 100 nm, B: 20 nm, C: 5 nm) and size distribution of MNPs (D).

The measuring parameters and the specificity of each measurement technique often result in different sizes for the same sample. Dynamic light scattering (DLS) is compared with transmission electron microscopy (TEM) for the characterization of the size distribution of magnetic nanoparticles. TEM measures the geometric size of dry MNPs deposited on a support surface under ultrahigh vacuum conditions. The DLS technique measures the hydrodynamic diameter that refers to how a particle diffuses within a liquid. Consequently, results obtained from DLS show a larger diameter than those from TEM. The significant difference in size between DLS and TEM results may be explained by an increased size in DLS due to the presence of the dispersant and the formation of hydrate layers. The presence of bigger particles and aggregates enhances light scattering and can also contribute to larger size values. Even though boundaries between particles in aggregates are not always obvious to recognize when analysing TEM images, the MNP size distribution observed by the TEM image-processing technique had a narrower range than that of DLS analysis.

Fig. 6 shows the pH dependence of the particle size and the zeta potential for 0.01% V/V MNPs in dH_2O. DLS reveals a hydrodynamic diameter of 250 nm at the current pH 7 of the MNP dispersion in dH_2O. The TEM image in Fig. 4A already suggests larger aggregates of primary nanoparticles, which maintain their assembly when dispersed in water. A pH titration was first performed from the native pH 7 to pH 11 using 0.1 mol/L NaOH (measurement 1). Above pH 8, the particle size shows a sudden increase and approaches a steady diameter of 3 μm at pH 9. At higher pH we observe the onset of a trend towards smaller size, but the scatter of data disables a firm conclusion on a decreasing diameter. The direction of the pH change was then reversed by a titration towards the acidic range using 0.1 mol/L HCl. The diameter of 3 μm remains down to pH 8 followed by a sudden decrease and an approach of the initial diameter of 250 nm at pH 5. Below pH 3 we may assume again the onset of a trend towards a small growth of the particle aggregates. Although the changes in the hydrodynamic diameter of the MNPs is obviously fully reversible, we observe a hysteresis of the evolution of particle size with pH between the titrations to high and low pH, respectively.

To understand the pH dependence of the particle size, the zeta potential of the MNPs was recorded in paral-

lel. The zeta potential is the key parameter that controls electrostatic interactions in particle dispersions, provides information about surface functionality and determines the dispersion stability. The zeta potential for particle dispersions is calculated from the measurement of the electrophoretic mobility by electrophoretic light scattering (ELS). At pH 7 a positive zeta potential of ζ = +30 mV was observed, which indicates a significant positive charge density at the nanoparticle-water interface and confirm the presence of the amine functional groups of the outermost APTMS coating of the core@shell maghemite nanoparticles. The amine groups get protonated in water and assume a positive charge.[39] When increasing the pH of the aqueous dispersion of the MNPs, the zeta potential decreases and approaches the isoelectric point (IEP) at pH 9.8. Beyond the IEP the zeta potential assumes a negative sign indicating the charge reversal of the MNPs. The IEP 9.8 is indicative for the moderately basic character of the aminosilane.[40] When continuing the pH titration from the alkaline to the acidic range, the zeta potential increases again and shows a charge reversal of the MNPs at a lower IEP 8.5. The electrokinetic charge density achieves a steady state indicated by the plateau value of the zeta potential of ζ = +35 mV below pH 5. We observe the same hysteresis for the pH dependence of the zeta potential and of the particle size when repeating the titration from high to low pH.

As a rule of thumb, a zeta potential below –25…–30 mV or above +25…+30 mV describes a stable dispersion where the aggregation of nanoparticles is suppressed by the electrostatic repulsion of particles with alike charge.[41] This empirical observation is confirmed by the correlation of the hydrodynamic diameter and the zeta potential of MNPs shown in Fig. 5.

As the initial zeta potential drops below ζ = +25 mV, the size of the MNPs starts to increase indicating the onset of the formation of larger aggregates. As the zeta potential approaches the IEP, the electrostatic repulsion between MNPs becomes weaker, and the average size of the particle aggregates, which remain suspended in dH_2O, obtains its maximum diameter of 3 μm. Above the IEP 9.8, the negative zeta potential steadily increases thereby introducing repulsive electrostatic forces between MNPs, which are now negatively charged. Since the zeta potential at pH 11 does not exceed the empirical threshold of ζ = ±25 mV, its effect on the disaggregation of particle assemblies remains rather small.

In the opposite direction of the pH titration, the threshold value of ζ = +25 mV is observed at pH 6.5 where the hydrodynamic diameter returns to 250 nm, which is the average size of the MNP aggregates in dH_2O. At very low pH, the significant volume of acid (0.1 mol/L HCl) added to decrease pH introduces a simultaneous increase in the ionic strength of the aqueous solution. Although the scatter of results in the range of pH 2.5–4 does not allow a conclusion on a decrease in the zeta potential, the electric double layer at the MNP-water interface gets suppressed at higher ionic strength, which again weakens the repulsive force between positively charged MNPs.

The hysteresis observed when repeating the analysis of the pH dependence of the zeta potential and the shift of the IEP from pH 9.8 (for the first titration) to pH 8.5 (for the second titration) indicate a decrease in the average basic strength of the functional coating of the MNPs. Obviously, the stability of the silane coating on the silica shell of the MNPs at higher pH is limited.

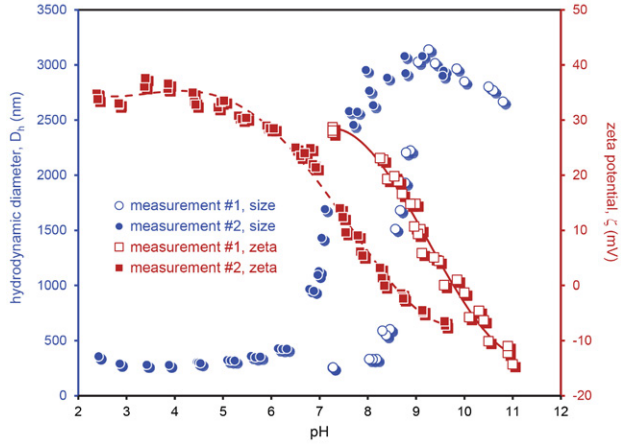

Figure 5: pH dependence of zeta potential and particle size for a dispersion of 0.01% V/V MNPs in dH_2O

3. 1. Adsorption of Nd^{3+} Ions

To elucidate the efficiency of Nd^{3+} ion adsorption on MNPs, an appropriate analytical method for quantification of the adsorption process was selected. The concentration of Nd^{3+} ions adsorbed on the MNP surface or the depletion of Nd^{3+} ion concentration in the aqueous solution may be determined. There have been many analytical techniques used for the determination of the REEs in solid and solution samples; flame or graphite furnace atomic absorption spectrometry, atomic absorption with chemical vapor generation, X-ray fluorescence spectrometry (XRF), inductively coupled plasma optical emission spectrometry (ICP-OES), inductively coupled plasma mass spectrometry (ICP-MS), high-performance liquid chromatography (HPLC) and neutron activation analysis (NAA).[41–43] Among the methods presented above for the characterization of various properties of the MNPs (composition, functional groups, size, charge), ATR FTIR and ELS may be considered to exhibit changes in the IR spectrum and in the zeta potential, respectively, of MNPs before and after adsorption of Nd^{3+} ions.

As shown in Fig. 3, the ATR FTIR spectrum of the core@shell MNPs after adsorption of Nd^{3+} ions indicates the presence of neodymium by the additional peak at 1307 cm^{-1}. The intensity of this peak compares with the peak indicating the N-H bending vibration (at 1627 cm^{-1}) and is likely assigned to a vibration of the assumed Nd-NH

surface complex that shows responsible for the adsorption of Nd^{3+} ions on the positively charged γ-Fe_2O_3-NH_4OH@SiO_2(APTMS) nanoparticles. Since the intensity of the peak at 1307 cm^{-1} is rather weak and a calibration protocol is thus not feasible to correlate peak intensity with Nd surface concentration, ATR FTIR is only applicable to qualitatively confirm the presence of Nd.

The zeta potential is occasionally applied to describe and to study the adsorption process of dissolved compounds such as surfactants, polymers (polyelectrolytes, polysaccharides), or proteins on material surfaces.[44–46] It is therefore feasible to investigate the capability of ELS for monitoring the adsorption of Nd^{3+} ions on MNPs although the same positive sign of the charge reduces the sensitivity of zeta potential analysis for the characterization of adsorption processes.

Table 1 shows the zeta potential of MNPs remaining in dispersion after an apparent separation by an external magnet followed by centrifugation and filtration with a 200 nm filter after adsorption of Nd^{3+} ions from aqueous solutions of $Nd(NO_3)_3$ with different bulk concentration (0.01, 0.025, 0.05 mol/L, respectively). The average zeta potential and the standard deviation were obtained from three repetitive measurements.

A steady decrease in the positive zeta potential was found from ζ = +47.7 ± 4.2 mV after adsorption from a 0.01 mol/L Nd^{3+} to ζ = +23.4 ± 2.4 mV when the initial concentration of Nd^{3+} ions was 0.05 mol/L. In the same series, the conductivity of the corresponding solutions increased from 406 mS/m to 1366 mS/m. The dependence of the zeta potential on the ionic strength is therefore dominating the decrease in the magnitude of the positive zeta potential of remaining MNPs in dispersion. Independent of the zeta potential and the ionic strength, the particle size remains at D_h = 80.5 ± 0.8 nm. This hydrodynamic diameter is significantly smaller than the size of D_h = 256 nm of the MNPs determined in the MNP stock solution in deionized water. The difference in the particle size is explained by the removal of the larger fraction of MNPs by filtration with a 200 nm filter. The zeta potential of the bulk dispersion of MNPs in dH_2O reads ζ = +28.2 ± 0.5 mV. This zeta potential is only 60% of the zeta potential determined in 0.01 mol/L $Nd(NO_3)_3$ (the lowest Nd^{3+} ion concentration used in the series of adsorption experiments) although the conductivity of the MNP bulk dispersion (18.4 mS/m) is much lower than the corresponding conductivity (406 mS/m) of 0.01 mol/L Nd^{3+}. If the diminishingly small ionic strength of deionized water is considered, the Hückel approach for the calculation of the zeta potential can be used, which transfers ζ = +28.2 mV determined in the Smoluchowski limit to ζ = +42.3 mV and therefore closer to the zeta potential obtained in the 0.01 mol/L Nd^{3+} solution. However, the conductivity of the bulk MNP dispersion of 18.4 mS/m is multiple times higher than the conductivity expected for dH_2O (theoretically 0.006 mS/m) indicating a significant contribution of the charged MNPs to the electric conductance of the aqueous dispersion. A conductivity of 18.4 mS/m corresponds to an ionic strength of approx. 0.001 mol/L when considering a monovalent electrolyte such as NaCl or KCl. This ionic strength justifies the application of the Smoluchowski approach for the calculation of the zeta potential especially when considering the average particle diameter of 256 nm. It can be concluded that either the influence of the particle size and/or the high concentration of MNPs in the bulk dispersion affect the electrophoretic mobility and thus the zeta potential.

In conclusion, the strong dependence of the zeta potential on the ionic strength does not qualify this method for the estimation of the surface concentration of adsorbed Nd^{3+} ions on the MNPs.

Table 1: Zeta potential (ζ) and hydrodynamic diameter (D_h) of MNPs after adsorption of Nd^{3+} ions from aqueous solution with different bulk concentration of $Nd(NO_3)_3$.

Nd^{3+} bulk concentration (mol/L)	Conductivity (mS/m)	ζ (mV)	D_h (nm)
0 *	18.4	28.2 ± 0.5	256
0.01	406	47.7 ± 4.2	81.3
0.025	906	34.1 ± 3.4	80.3
0.05	1366	23.4 ± 2.4	79.8

* MNPs dispersed in dH_2O, i.e., without separation

For monitoring the depletion of Nd^{3+} ions in solution upon adsorption on MNPs, the optical properties of aqueous solutions of this REE suggest the application of UV-Vis spectroscopy. Fig. 6 shows the UV-Vis spectrum of aqueous solutions of $Nd(NO_3)_3$ at different concentration (0.01, 0.025, 0.05 mol/L, respectively) in the wavelength range of 540–780 nm. In this range we find two distinct absorption peaks at 575 nm and 740 nm, which may be assigned to the electronic f-f transitions $^4I_{9/2} \rightarrow {}^2G(1)_{7/2}$ and $^4G_{5/2}$ (575 nm, 17391 cm^{-1}) and $^4I_{9/2} \rightarrow {}^4F_{7/2}$ (740 nm, 13514 cm^{-1}).[47] The absorbance recorded at these peaks was used to establish calibration curves for the estimation of the Nd^{3+} ion concentration from the measured absorbance after completing the adsorption process on MNPs. The corresponding calibration curves are shown in the inset of Fig. 6. Coincidently at a given Nd^{3+} concentration, the peaks at 575 nm and 740 nm show almost the same absorbance.

Fig. 6 also shows the UV-Vis spectra obtained after adsorption of Nd^{3+} on MNPs in solutions with the corresponding Nd^{3+} starting concentration (0.01, 0.025 and 0.05 mol/L, respectively) after separation of the MNPs by an external magnet, centrifugation and filtration using a

filter with 200 nm pores. We do not find any decrease in the absorbance for both f-f transition peaks, which suggests that adsorption of Nd^{3+} ions on γ-Fe_2O_3-NH_4OH@SiO_2(APTMS) nanoparticles did not occur. However, upon filtration of the supernatant obtained after centrifugation of the MNP dispersion, that is remaining after applying an external magnet, with a 20 nm filter, the absorbance decreases consistently for the peaks at both 575 nm and 740 nm. The evaluation of the depletion of Nd^{3+} from the stock solution using the UV-Vis calibration curves reveals a removal of 30% at pH 7 and after 3 h of interaction time. DLS and ELS measurements of the filtrate still show clear distributions of size and zeta potential with D_h = 51 nm and ζ = +17.8 ± 1.8 mV. We note that (i) small aggregates of primary MNPs pass the 20 nm filter and (ii) the filter shows a small rejection at the nominal threshold of 20 nm. The measured conductivity in the filtrate reads 1176 mS/m, which is 14% lower than the conductivity in the filtrate of the 200 nm filter. We may thus assume a larger zeta potential but observe the opposite. Obviously, the different size fractions of MNPs exhibit different effective charge density represented by the difference in the zeta potential. The presence of MNPs in the filtrate of the 20 nm filter suggests a contribution of Nd^{3+} adsorbed on these MNPs to the UV-Vis absorption spectrum. The removal efficiency is therefore expected slightly higher than the estimated 30%.

4. Conclusions

Magnetic nanoparticles with a γ-Fe_2O_3 core, coated with SiO_2 and functionalized with APTMS, were synthesized with the purpose of removing rare earth elements from aqueous solutions. The main reason for selecting Nd^{3+} as the source of REE is the fact that neodymium is one of the most important REE in terms of usage and applicability. Furthermore, neodymium is among those REEs that show a lot of absorption peaks in the visible spectrum, which makes UV-Vis absorption spectroscopy convenient for the determination of the Nd^{3+} concentration in solution. The synthesized MNPs were characterized in terms of size (TEM, DLS), charge (zeta potential; ELS), surface functionality (ATR-FTIR), and composition (TGA, XRD). The adsorption of Nd^{3+} on γ-Fe_2O_3-NH_4OH@SiO_2(APTMS) was performed in batch mode. The UV-Vis calibration curves revealed maximum adsorption to be 30% at pH 7, with use of 12 mg of MNPs in 0.05 mol/L of neodymium solution. Based on the results, an obvious decrease in neodymium concentration becomes visible only after a reaction time of 3 hours, which makes this process uneconomical for large-scale use. The removal of γ-Fe_2O_3-NH_4OH@SiO_2(APTMS) from dispersion after Nd^{3+} adsorption requires multiple steps (removal with a magnet, centrifugation, and filtration) in order to measure the absorbance spectrum without a significant interference of MNPs remaining in the processed solution, which also requires time and adds additional steps to the process. Ban et al. reported the use of ultrafiltration to completely remove even the primary particles of MNPs.[48] The slow

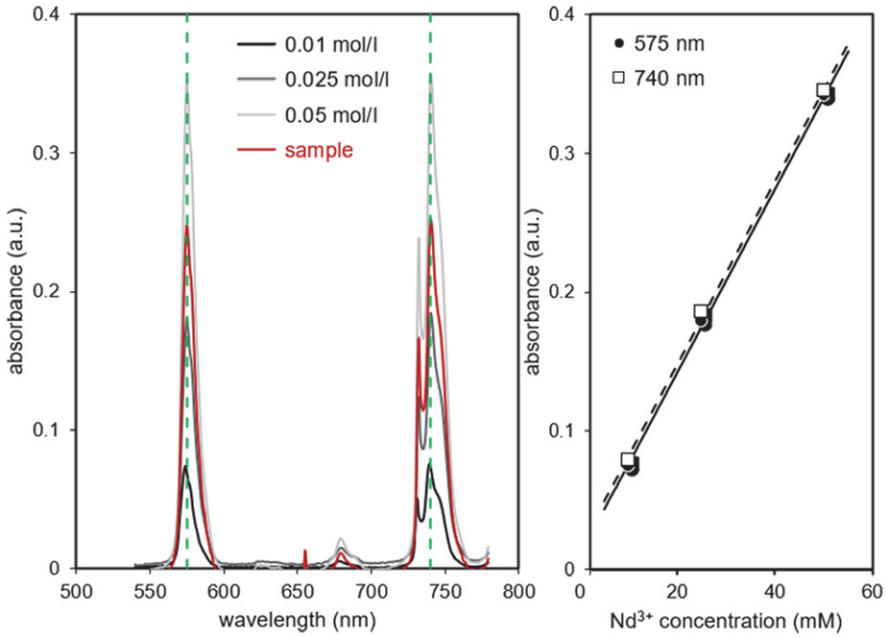

Figure 6: Absorbance spectra of Nd^{3+} before and after adsorption on MNPs. The labels of spectra recorded after adsorption indicate the filter used for removing MNPs (pore size 20 nm, 200 nm).

From the change in the absorbance for MNPs filtered with a 20 nm filter after adsorption of 0.05 M Nd^{3+}, we conclude that 0.035 M Nd^{3+} remain in solution. The adsorption efficiency after 3 hours is therefore 30%.

adsorption of Nd^{3+} ions on γ-Fe_2O_3-$NH_4OH@SiO_2$ (APTMS) suggests a coating by different chelating compounds, such as polyethylenimine or negatively charged MNPs.[34]

Acknowledgements

The authors acknowledge dr. Julija Volmajer Valh for her help with ATR-FTIR, dr. Sašo Gyergyek for TEM analysis, Edi Kranjc for XRD analysis, and dr. Karl Gatterer of Graz University of Technology for donating Nd_2O_3.

5. References

1. D. A. Atwood: The rare earth elements: Fundamentals and Applications, John Wiley & Sons Ltd, **2012,** pp. 2–27.
2. J. H. L. Voncken: The Rare Earth Elements: An Introduction, Springer, **2016**, pp. 1–11. **DOI:**10.1007/978-3-319-26809-5
3. U.S. department of Energy, Critical Materials Strategy, https://www.energy.gov/sites/prod/files/DOE_CMS2011_FINAL_Full.pdf, (accessed: February 18, 2022)
4. V. Balaran, *Geosci. Front.,* **2019**, *10*, 1285–1303. **DOI:**10.1016/j.gsf.2018.12.005
5. C. E. D. Cardoso, J. C. Almeida, C. B. Lopes, T. Trindade, C. Vale and E. Pereira, *Nanomater.,* **2019**, *9*, 1–55. **DOI:**10.3390/nano9060814
6. K. Binnemans, P. T. Jones, B. Blanpain, T. Van Gerven and Y. Pontikes, *J. Clean. Prod.,* **2015***, 99*, 17–38. **DOI:**10.1016/j.jclepro.2015.02.089
7. R. Ashour, R. Elsayed, A. F. Abdel-Magied, K. M. Forsberg, A. Uheida and M. Muhammed, *Chem. Eng. J.,* **2017,** *327*, 286–296. **DOI:**10.1016/j.cej.2017.06.101
8. A. Negrea, A. Gabor, C. M. David, M. Ciopec, P. Negrea, N. Duteanu and A. Barbulescu, *Sci. Rep.,* **2018**, *8*, 1–11. **DOI:**10.1038/s41598-017-18623-0
9. M. A. Agotegaray, V. L. Lassalle: Silica-coated Magnetic Nanoparticles: An Insight into Targeted Drug Delivery and Toxicology, Springer, **2017,** pp. 12–24. **DOI:**10.1007/978-3-319-50158-1
10. L. L. Vatta, R. D. Sanderson, K. R. Koch, *Pure Appl. Chem.,* **2006***, 78*, 1793–1801. **DOI:**10.1351/pac200678091793
11. T. Kegl, A. Košak, A. Lobnik, I. Ban, Z. Novak and A. Kovač Kralj, *J. Hazard. Mater.,* **2019**, *386*, 1–59. **DOI:**10.1016/j.jhazmat.2019.121632
12. S. Majidi, F. Zeinali Sehrig, S. Mussa Farkhani, M. Soleymani Goloujeh, A. Akbarzadeh, *Artif. Cells Nanomed. Biotechnol.,* **2016***, 44*, 722–734. **DOI:**10.3109/21691401.2014.982802
13. Y. Bao, T. Wen, A. C. S. Samia, A. Khandhar, K. M. Krishnan, *J. Mater. Sci.,* **2016***, 51*, 513–553. **DOI:**10.1007/s10853-015-9324-2
14. M. Sharma, P. Kalita, K. K. Senapati, A. Garg: Study on Magnetic Materials for Removal of Water Pollutants, **2018,** 61–78. **DOI:**10.5772/intechopen.75700
15. N. Zhu, H. Ji, P. Yu, J. Niu, M. U. Farooq, M. Waseem Akram, I. O. Udego, H. Li, X. Niu, *Nanomater.,* **2018**, *10,* 1–27.
16. P. Xu, G. M. Zeng, D. L. Huang, C. L. Feng, S. Hu, M. H. Zhao, C. Lai, Z. Wei, C. Huang, G. Xin Xie and Z. Feng Liu, *Sci. Total Environ.,* **2012***, 424*, 1–10. **DOI:**10.1016/j.scitotenv.2012.02.023
17. S. P. Gubin: Magnetic Nanoparticles, Wiley-VCH, **2009,** 25–58. **DOI:**10.1002/9783527627561
18. A. Jurgec, Funkcionalizirani magnetni nanodelci za odstranjevanje težkih kovin iz odpadnih vod, https://dk.um.si/IzpisGradiva.php?id=74201&lang=slv. (accessed: February 20, 2022)
19. I. Ali, C. Peng, I. Naz and M. A. Amjed: Magnetic Nanostructures, Springer, **2019**, 161–179.
20. J. Kudr, Y. Haddad, L. Richtera, Z. Heger, M. Cernak, V. Adam, O. Zitka, *Nanomater.*, **2017**, *9,* 1–28.
21. A. M. Gutierrez, T. D. Dziubla, J. Z. Hilt, *Rev. Environ. Health,* **2017***, 32*, 111–117. **DOI:**10.1515/reveh-2016-0063
22. O. Pereao, C. A. Bode-Aluko, O. Fatoba, K. Laatikainen, L. F. Petrik, *Desalination Water Treat.,* **2018***, 130*, 71–86. **DOI:**10.5004/dwt.2018.22844
23. D. Dupont, W. Brullot, M. Bloemen, T. Verbiest and K. Binnemans, *ACS Appl. Mater. Interfaces.,* **2014**, *7*, 4980–4988. **DOI:**10.1021/am406027y
24. O. Plohl, U. Ajdnik, S. Gyergyek, I. Ban, A. Vesel, T. Kraševac Glaser, L. Fras Zemljič, *J. Environ. Chem. Eng.,* **2019***, 7,* 6777–6789. **DOI:**10.1016/j.jece.2019.102913
25. O. Plohl, M. Finšgar, S. Gyergyek, U. Ajdnik, I. Ban and L. Fras Zemljič, *Nanomater.,* **2019***, 209,* 1–20. **DOI:**10.3390/nano9020209
26. R. M. Ashour, R. El-sayed, A. F. Abdel-Magued, A. A. Abdel-khalek, M. M. Ali, K. Forsberg, A. Uheida, M. Muhammed and J. Dutta, *J. Chem. Eng.,* **2017**, *327,* 286–296. **DOI:**10.1016/j.cej.2017.06.101
27. D. Dupont, J. Luyten, M. Bloemen, T. Verbiest and K. Binnemans, *Ind. Eng. Chem. Res.,* **2014***, 53,* 15222–15229. **DOI:**10.1021/ie502546c
28. A. A. Galhoum, M. G. Mafhouz, S. T. Abdel-Rehem, N. A. Gomaa, A. A. Atia, T. Vincent and E. Guibal, *Nanomater.,* **2015***, 5*, 154–179. **DOI:**10.3390/nano5010154
29. A. A. Galhoum, M. G. Mafhouz, S. T. Abdel-Rehem, N. A. Gomaa, A. A. Atia, T. Vincent and E. Guibal, *Cellulose.,* **2015,** *22,* 2589–2605. **DOI:**10.1007/s10570-015-0677-0
30. C. Gok, *J. Radioanal. Nucl. Chem.,* **2014,** *301*, 641–651. **DOI:**10.1007/s10967-014-3193-z
31. J. Li, A. Gong, F. Li, L. Qiu, W. Zhang, G. Gao, Y. Liu and J. Li, *RSC Adv.*, **2018,** *68,* 39149–39161.
32. E. Liu, X. Zheng, X. Xu, F. Zhang, E. Liu, Y. Wang, C. Li and Y. Yan, *NJC,* **2017***, 15,* 7739–7750. **DOI:**10.1039/C7NJ02177A
33. A. Miraoui, M. A. Didi and D. Villemin, *JRNC,* **2016,** *307***,** 963–971**. DOI:**10.1007/s10967-015-4267-2
34. L. Molina, J. Gaete, I. Alfaro, V. Ide, F. Valenzuela, J. Parada and C. Basualto, *J. Mol. Liq.,* **2019**, *275,* 178–191. **DOI:**10.1016/j.molliq.2018.11.074
35. S. D. Topel, E. Polido Legaria, C. Tiseanu, . J. Rocha, J.-M. Nedelec, . V. G. Kessler and . G. A. Seisenbaeva, *J. Nanoparticle Res.,* **2014***, 2783*.
36. V. Rocher, J. Manerova, M. Kinnear, D. J. Evans, *Dalton Trans.,* **2014***, 43*, 2948–2952. **DOI:**10.1039/C3DT52386A

37. P. Melnikov, I. V. Arkhangelsky, V. A. Nascimento, L. C. S. de Oliveira, G. A. Wandekoken, D. Muniz de Albuquerque, *J. Therm. Anal. Calorim.,* **2019,** 1117–1121.
38. J. G. Smith: Organic Chemistry, McGraw-Hill, 3rd edition, **2011**, pp. 1075–1086.
39. P. Nygård, . K. Grundke, E. Mäder, C. Bellmann, *J. Adhes. Sci. Technol.,* **2002,** *16*, 1781–1808. **DOI:**10.1163/156856102320396148
40. T. Luxbacher: The Zeta Potential for Solid Surface Analysis, Anton Paar GmbH, **2014,** pp. 10–138.
41. B. Zawisza, K. Pytlakowska, B. Feist, M. Polowniak, A. Kita, R. Sitko, *J. Anal. At. Spectrom.,* **2011***, 26,* 2373–2390. **DOI:**10.1039/c1ja10140d
42. A. Anggraeni, F. Arianto, A. Mutalib, U. Pratomo, H. H. Bahti: Mathematics, Science, and Computer Science Education (MSCEIS 2016): AIP Conf. Proc., **2017**.
43. E. Zolfonoun, S. R. Yousefi, *J. Braz. Chem. Soc.*, **2016**, *27,* 1–6.
44. Z. Adamczyk, M. Nattich, M. Wasilewska, M. Zaucha, *Adv. Colloid Interface Sci.,* **2011**, *168*, 3–28. **DOI:**10.1016/j.cis.2011.04.002
45. J. Ethève and P. Déjardin, *Langmuir,* **2002***, 18*, 1777–1785. **DOI:**10.1021/la011224d
46. C. Payerl, M. Bračič, A. Zankel, W. J. Fischer, M. Kaschowitz, E. Fröhlich, R. Kargl, F. Stelzer, S. Spirk, *Carbohydr. Polym.,* **2017***, 164*, 49–56. **DOI:**10.1016/j.carbpol.2017.01.088
47. P. Caro, D. R. Svoronos, E. Antic, M. Quarton, *J. Chem. Phys.,* **1977**, *66,* 215–220. **DOI:**10.1063/1.433910
48. I. Ban, S. Markuš, S. Gyergyek, M. Drofenik, J. Korenak, C. Helix-Nielsen, I. Petrinić, *J. Nanomater.,* **2019***, 9,* 1–17. **DOI:**10.3390/nano9091238

Povzetek

Magnetni nanodelci (MNP) so zaradi svoje hitre sinteze, vsestranske funkcionalizacije in možnosti recikliranja z uporabo magnetnega polja deležni vse večje pozornosti za različne aplikacije. Visoko razmerje med površino in prostornino disperzij MNP predstavlja zmožnost njihove uporabe kot adsorbenta za odstranjevanje ionov težkih kovin. Raziskali smo uporabnost MNP, sestavljenih iz maghemitnega jedra in obdanih s kremenčevo lupino, funkcionalizirano z aminopropilsilanom, γ-Fe_2O_3-NH_4OH@SiO_2 (APTMS), za odstranjevanje neodimovih ionov (Nd^{3+}) iz vodne raztopine. MNP so bili karakterizirani glede na velikost, sestavo, površinsko funkcionalnost in naboj. Kljub obetavnim lastnostim MNP pa njihova odstranitev iz vodne disperzije z zunanjim magnetom ni zadostovala za zanesljivo kvantificiranje adsorpcije Nd^{3+} z UV-Vis spektroskopijo.